Visualizing choriocapillaris using swept source optical coherence tomography angiography with various probe beam sizes

Zhou, Kanheng; Song, Shaozhen; Zhang, Qinqin; Chu, Zhongdi; Huang, Zhihong; Wang, Ruikang K.

Published in:
Biomedical Optics Express

DOI:
10.1364/BOE.10.002847

Publication date:
2019

Research Article | Vol. 10, No. 6 | 1 Jun 2019 | BIOMEDICAL OPTICS EXPRESS 2847
Biomedical Optics EXPRESS

Visualizing choriocapillaris using swept-source optical coherence tomography angiography with various probe beam sizes

KANHENG ZHOU,[1,2] SHAOZHEN SONG,[2] QINQIN ZHANG,[2] ZHONGDI CHU,[2] ZHIHONG HUANG,[1] AND RUIKANG K. WANG[2,3,*]

[1]School of Science and Engineering, University of Dundee, Dundee DD1 4HN, UK
[2]Department of Bioengineering, University of Washington, Seattle, WA 98195, USA
[3]Department of Ophthalmology, University of Washington, Seattle, WA 98195, USA
*wangrk@uw.edu.

Abstract: Imaging choriocapillaris (CC) is a long-term challenge for commercial OCT angiography (OCTA) systems due to limited transverse resolution. Effects of transverse resolution on the visualization of a CC microvascular network are explored and demonstrated in this paper. We use three probe beams with sizes of ~1.12 mm, ~2.51 mm and ~3.50 mm at the pupil plane, which deliver an estimated transverse resolution at the retina of 17.5 μm, 8.8 μm and 7.0 μm, respectively, to investigate the ability of OCTA to resolve the CC capillary vessels. The complex optical microangiography algorithm is applied to extract blood flow in the CC slab. Mean retinal pigment epithelium (RPE) to CC (RPE-CC) distance, mean CC inter-vascular spacing and the magnitude in the radially-averaged power spectrum are quantified. We demonstrate that a clearer CC lobular capillary network is resolved in the angiograms provided by a larger beam size. The image contrast of the CC angiogram with a large beam size of 3.50 mm is 114% higher than that with a small beam size of 1.12 mm. While the measurements of the mean RPE-CC distance and CC inter-vascular spacing are almost consistent regardless of the beam sizes, they are more reliable and stable with the larger beam size of 3.50 mm. We conclude that the beam size is a key parameter for CC angiography if the purpose of the investigation is to visualize the individual CC capillaries.

1. Introduction

Choriocapillaris (CC) is a monolayer vascular network of lobularly arranged continuous capillaries located in the innermost layer of the choroid between Bruch's membrane (BM) and Sattler's layer [1]. Histological studies have indicated a close relationship between the changes in the CC integrity and the multiple ocular diseases such as age-related macular degeneration [2,3], diabetic retinopathy [4] and glaucoma [5]. Therefore, an ability of detecting and monitoring the changes in the CC integrity would be important to help understand the disease pathologies that involve the CC, and subsequently improve their diagnosis and therapeutic intervention.

Optical coherence tomography angiography (OCTA) is now a well-established noncontact and noninvasive imaging technique that utilizes repeated B-scans at the same location to discriminate blood flow motion from a static tissue bed with micrometer-level spatial resolution [6,7]. Recently, the use of OCTA for CC imaging has drawn significant attention in the research and clinical community [8–17]. Gorczynska *et al.* [13] reported successful in-vivo CC imaging using a 1.7 MHz A-line rate swept-source OCT (SS-OCT) system with a transverse resolution of 14 μm. The ultrahigh A-line rate enabled up to 3.5x oversampling (4 μm/pixel) in the lateral direction with a large number of repeated B-scans (20 total repeats for a bidirectional scan, 10 forward and 10 backward), resulting in significant reduction of the remaining background static tissue noise caused by the motion and unstable phase in the CC

#359116 https://doi.org/10.1364/BOE.10.002847
Journal © 2019 Received 30 Jan 2019; revised 2 Apr 2019; accepted 9 May 2019; published 16 May 2019

Biomedical Optics EXPRESS

imaging. Kurokawa *et al.* [14] demonstrated CC angiography showing individual CC microvessels using adaptive optics OCT (AO-OCT). The Shack-Hartmann wavefront sensor and deformable lens in the AO-OCT system corrected the aberration induced by the imperfection of the optics in the eye, which gave the AO-OCT system a high transverse resolution of 2.4 µm for better CC visualization. While very promising, these investigations are only achievable by research OCTA systems, which are not necessarily useful for clinical studies.

There are numerous reports that utilize commercial OCTA systems to quantify the CC in both normal and diseased eyes, e.g [16–26], which are important because of their obvious clinical impacts that could be brought to the community. Current commercial systems for such purpose typically have an imaging speed of 100-200 kHz A-line rate with 15-25 µm transverse resolution. However, the CC at the posterior pole (central macular region) is a much denser network with an averaged intercapillary-distance (ICD) between 10 – 25 µm [27], similar to the size of the system transverse resolution. Therefore, it is almost impossible for commercial systems to resolve individual capillaries under the posterior pole currently. For this reason, researchers have opted for an alternative strategy to quantify the CC by evaluating the flow deficits, together with post-image processing methodologies [16,17,20]. This makes sense because a flow deficit by its definition must have a size that is larger than the normal ICD, which is within the capability of the system to resolve. Zhang *et al.* [16] reported highly repeatable in-vivo assessment of CC angiography using a PLEX Elite 9000 SS-OCTA system from Carl Zeiss Meditec, Inc., where intensity compensation was applied on resultant CC angiograms to compensate the potential shadowing effect caused by the RPE complex, thus improving the CC image quality for evaluating the flow deficits. On the same system, Chu *et al.* [17] demonstrated high contrast CC angiograms at different retinal locations from macular to equatorial regions on six subjects, where a three-step registration and averaging approach was employed with five repeated volume scans to suppress the remaining background static tissue noise, thus increasing the contrast of CC OCTA images for the purpose of visualization and quantification. However, due to the limitation in the system transverse resolution, it is truly difficult for commercial systems to visualize the individual capillaries at the posterior pole. Such limitation is brought by the small probe beam size that enters the eye, leading to a relatively large focused beam spot at the retina. According to Gaussian optics however, the transverse resolution (or focused beam spot size) is proportional to the numerical aperture (NA) of the probe beam system, where a probe beam entering the eye with a larger size would lead to a tighter focused beam spot at the retina, thus the higher transverse resolution. Although this is a commonly known concept, and several recent studies [28–30] have demonstrated improved retinal vascular visualization using a OCT system with a relatively large beam size (about 3 mm) and a simplified adaptive optics setup, there is no investigation conducted so far to explore the effect of transverse resolution on the CC visualization using a conventional OCT without employing adaptive optics for potential aberration correction.

In this study, we explored and demonstrated the effect of system transverse resolution on CC microvascular imaging by various NA settings of the objective optics, in an attempt to visualize the CC capillary network under the posterior pole region. We used a number of morphometric parameters, such as mean RPE-CC distance, mean CC inter-vascular spacing and magnitude of the radially-averaged power spectrum, to assess the resulting CC OCTA *en-face* images.

2. Materials and methods

2.1 SS-OCT system for CC imaging

A prototype research SS-OCT system with features similar to commercially available 1.0-µm-center-wavelength SS-OCTA systems was employed in this study for the investigation of how the incident beam size at the pupil plane would have an effect on CC imaging. The simplified system schematic is shown in Fig. 1(A), which was based on a fiber-based

Biomedical Optics EXPRESS

Michelson interferometer. A 200 kHz MEMS-tunable swept source laser (AXP50124-3, AXSUN Technologies Inc., Billerica, MA, USA, 1051 nm central frequency, 105.2 nm bandwidth) was used as the light source. A 75:25 beam splitter was applied in the system to deliver 75% laser light into the reference arm and 25% to the sample arm. The reference arm contained an optical delay line and a three-paddle polarization controller. The polarization controller applied in this system was used to match the polarization state of the light in both reference and sample arm, and thus to maximize the interference intensity to increase the system sensitivity. The sample arm consisted of a collimator, a 2D galvo-scanner, a scan lens and an ophthalmic lens. The scan lens and ophthalmic lens were in 4f configuration. There were three different configurations for the collimator, scan lens and ophthalmic lens in the sample arm to deliver incident beam with various diameters (see section 2.2 for details). A built-in balanced photodetector was used to collect the interferogram generated by the light from reference arm and the light backscattered from the sample. The signal from the balanced photodetector was then collected by a custom LabVIEW program (LabVIEW 2016, National Instruments, Austin, TX, USA) for post-processing. The system sensitivity was measured to be 105.3 dB at the incident beam intensity of 3.5 mW with a beam size of 2.51 mm by using a phantom eye with a mirror in the air. This value was slightly higher than that of theoretical maximum sensitivity (103.5 dB at the incident beam intensity of 3.5 mW), largely due to the neutral density filter used in our measurement that was not optimized for 1.06 μm center wavelength.

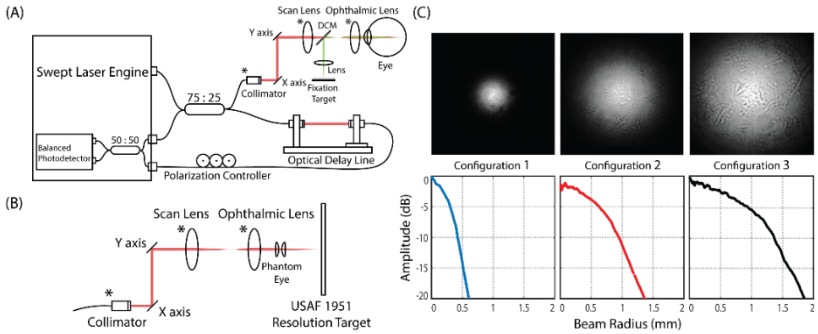

Fig. 1. Experimental arrangements to demonstrate the effect of the probe beam size on the ability to resolve the capillary vessels in the CC layer. (A) Experimental setup for CC imaging using SS-OCT system. There are three different configurations for the components denoted by star (*) in the sample arm for delivering a beam with various diameters into the eye. DCM: dichroic mirror. (B) Experimental setup for system transverse resolution measurement. A pair of convex lenses (0.5-inch diameter, 16.5 mm equivalent focal length) was used as a phantom eye to focus the beam onto USAF 1951 resolution target. System transverse resolution was then evaluated on the resulting images of the resolution target pattern. (C) Measured two-dimensional beam intensity maps (first row, gray scale) and their corresponding radially-averaged profiles (second row, line charts) of three different sample arm configurations.

The OCT axial resolution Δz is defined as the full width at half maximum (FWHM) of the source self-coherence length, which only depends on the center wavelength and bandwidth of the laser source (Eq. (1) [31]:

$$\Delta z = \frac{2\ln 2 \cdot \lambda_c^2}{\pi \cdot \Delta\lambda} \tag{1}$$

where λ_c, $\Delta\lambda$ denotes the center wavelength and the bandwidth of the laser source. With the center wavelength of the light source being 1051 nm and the spectral bandwidth of the light source being 105.2 nm, the nominal axial resolution of the system was calculated to be 4.6 μm in air with axial pixel sampling at 5.8 μm/pixel, corresponding to 3.3 μm in retinal tissue with axial pixel sampling at 4.2 μm/pixel (refraction index n = 1.38 [32]).

Biomedical Optics EXPRESS

According to Gaussian optics, the OCT transverse resolution Δx depends on the NA of the objective lens (human eye in this case), which can be estimated by following equation [33]:

$$\Delta x = \frac{1.22 \cdot \lambda_c}{2 \cdot NA_{obj}} = \frac{1.22 \cdot \lambda_c \cdot f_{eye}}{D} \quad (2)$$

We approximated NA_{obj} with $D/(2 \cdot f_{eye})$, where D denotes the incident beam diameter at the pupil (assuming the pupil is of sufficient size that does not block the incident light), and f represents the equivalent focal length of the eye (f_{eye} ≈16.6 mm). The OCT transverse resolution on the retina can thus be controlled by applying the incident beam with different beam sizes at the pupil plane.

2.2 Sample arm configuration

To image the CC with various OCT transverse resolution, three different lens configurations were implemented in the sample arm to deliver the probe beam with varied diameters, as shown in Table 1. The largest theoretical beam diameter (3.54 mm) was achieved by using a scan lens of 54 mm focal length and an ophthalmic lens of 58 mm focal length with a collimated beam of 3.3 mm in diameter. While the smallest theoretical beam diameter (1.16 mm) was realized by using a scan lens of 54 mm focal length and an ophthalmic lens of 26 mm focal length with a collimated beam of 2.4 mm in diameter.

The actual beam size of each configuration was then measured by a homemade beam profiler (UC20MPD, Spinel USA LLC., Irvine, CA, USA). The measured two-dimensional (2D) beam intensity maps in gray scale and their corresponding radially-averaged one-dimensional (1D) beam profiles with −20 dB cut-off were shown in Fig. 1(C). The $1/e^2$ probe beam widths (−17.4 dB cut-off width) before entering the eye were measured to be 1.12 mm, 2.51 mm and 3.50 mm, respectively, which agreed well with the theoretical calculations, as shown in Table 1.

Table 1. Detailed parameters for each sample arm configuration

Sample arm configuration	1	2	3
Scan lens f (mm)		54	
Ophthalmic lens f (mm)	26	58	58
Collimated beam size (mm)	2.4	3.3	3.3
Theoretical output beam size (mm)	1.16	2.58	3.54
Measured output beam size (mm)	1.12	2.51	3.50

To evaluate the actual system transverse resolution of each lens configuration, a U.S. Air Force test target (1951 USAF, Edmund Optics Inc., Barrington, NJ, USA) was imaged using all three lens configurations in the air. The experimental setup is shown in Fig. 1(B). A phantom eye with similar equivalent focal length of human eye (consisted of two 30 mm focal-length convex lens with 5.4 mm center distance, equivalent focal length of 16.5 mm) was employed as the objective lens to focus the incident beam onto the resolution target. To eliminate the error introduced by sampling, a high scan density was applied for imaging the resolution pattern of the groups 4 to 7 on the USAF test chart.

2.3 Imaging protocol

Four healthy subjects with no history of ocular disease were recruited for this study, as shown in Table 2. The average age was 36 years old, ranging from 28 to 54 years old. The use of a homebuilt SS-OCT system was approved by the Institutional Review Board of University of Washington, and the protocols adhered to the tenets of the Declaration of Helsinki. The intensity of the incident OCT beam was about 3.5 mW at the cornea and within the safe limits established by the American National Standards Institute (ANSI) [34].

Biomedical Optics EXPRESS

A desk-mounted ophthalmic chin rest was utilized to align and stabilize subjects' eye and head during imaging. The random eye drifts and saccades of subjects were minimized by using a fixation target in the sample arm (Fig. 1(A)). Before OCT data acquisition, the focus of the probe beam was optimized for CC visualization, which was realized by maximizing the image intensity at the RPE layer.

Table 2. Details of the 4 healthy subjects

Subject ID	Age	Gender	Refractive error		Eye imaged
			Sphere	Cylinder	
1	28	M	- 6.25 D	+ 1.00 D	Right
2	29	M	0 D	0 D	Right
3	32	F	- 1.75 D	- 0.75 D	Right
4	54	M	0 D	0 D	Right

For each subject, two repeated OCT volumes were acquired using the incident beam with beam diameter of 3.50 mm at the central fovea with each covering an image range of 2° × 2.6° (0.6 mm × 0.8 mm, width × height). For Subject 1, four additional OCT volumes were also acquired with smaller beam diameters (1.12 mm and 2.51 mm) for the purpose of demonstrating the effect of NA on the CC OCTA imaging. Each OCT volume consisted of 400 A-scans × 1600 B-scans with 4 repeated B-scans at the same location. The pixel pitch of each OCT volume was thus approximated to be 1.5 μm horizontally and 2 μm vertically, providing an oversampling ratio of ~8.8x for the beam diameter of 1.12 mm, ~4.4x for the beam diameter of 2.51 mm and ~3.5x for the beam diameter of 3.50 mm. Therefore, the sampling density was high enough to meet the Nyquist–Shannon sampling theorem even for imaging with largest beam diameter (highest transverse resolution). The SS-OCT system was operated at a B-scan rate of 330 Hz, resulting in a volume acquisition time of 4.8 s, which was tolerable for the patient imaging. All the data acquisitions were performed in a room with low environment light to ensure the pupil is sufficiently opened for collecting all the incident light. No dilation drops were applied to the subject in this study.

2.4 En-face CC OCTA projection and morphometric parameter quantification

The post-processing of the acquired OCT volumes was performed using custom MATLAB scripts (MATLAB 2018a, MathWorks Inc, Natick, MA, USA). The complex optical microangiography (OMAG) algorithm [11] was applied to extract blood flow information from the raw OCT volumes. A semi-automated segmentation algorithm [35] was then employed to perform layer segmentations and necessary motion corrections. After the layer segmentation and RPE layer flattening, the cross-sectional OCT and OCTA images were then averaged along the lateral direction to obtain the averaged depth profiles. Figure 2(A) shows a typical example of the flattened OCT and OCTA cross-sectional images. The corresponding normalized mean OCT (black solid line) and OCTA (red solid line) depth profiles are shown on the right (Fig. 2(B)). The small peaks above the IS/OS segment junction in the OCTA profile indicated the location of retinal vessels. The proximal retina layer was thus defined as a ~170 μm slab from the inner limiting membrane (retina top edge) to ~50 μm above the IS/OS segment junction. The peak in the OCTA profile just below the RPE peak (the third peak in the OCT profile) was identified as the location of the CC vessels. The CC layer was then defined as a 16 μm (4 pixels) thin slab, starting at the peak in the OCTA profile (17 – 20 μm below RPE layer). *En-face* retina and CC OCTA images were thus generated by sum projection [36] and displayed in a log scale, as shown in Fig. 2(C). Finally, both images were cropped to square areas external to the vertexes of the foveal avascular zone (FAZ) (yellow dashed frames in Fig. 2(C)) for further comparison and morphology analysis.

Several morphometric parameters were applied to quantify the final cropped *en-face* CC OCTA images, including mean RPE-CC distance, mean CC inter-vascular spacing (i.e., intercapillary distance), and magnitude of radially-averaged power spectrum of the CC image.

Biomedical Optics EXPRESS

Mean RPE-CC distance: the RPE-CC distance was defined as the axial distance between the RPE layer (the third peak in the OCT profile, Fig. 2(B) and the CC layer (peak in the OCTA profile, Fig. 2(B)). Its mean distance was calculated by averaging RPE-CC distances across the whole OCTA volume. This parameter is important to indicate the oxygen and metabolic exchange efficiency between the CC and overlying RPE. For example, a larger mean RPE-CC distance may inhibit efficient delivery of oxygen from the CC to photoreceptors [37].

Mean CC inter-vascular spacing: the mean CC inter-vascular spacing was defined as the average normal distance between two adjacent CC vessels, which is a key parameter to evaluate the CC normality. To quantify this parameter, 2D power spectrum analysis [13,14] was performed on the cropped *en-face* CC angiogram(Fig. 2(D)). Since the CC under the FAZ is a dense and regular-spaced lobular network of vessels, a concentration of energy at a consistent radial range in the 2D power spectrum is expected. The ring around the center point represents the spatial frequency components of visible CC network. The corresponding 1D normalized radially-averaged power spectrum is shown in Fig. 2(E) on the left side. The base line offset was removed by subtracting the power function fitted line from the originally biased spectrum. The compensated power spectrum that resulted is shown on the right side of Fig. 2(E). The mean CC inter-vascular spacing can then be considered as the inverse of the CC spatial frequency. To extract the spatial frequency of CC more accurately, the compensated CC power spectrum was fitted into a Gaussian function. The center of the Gaussian function was then regarded as the CC spatial frequency.

Magnitude of radially-averaged power spectrum: the magnitude of the peak in radially-averaged power spectrum was defined as the amplitude of the fitted Gaussian function (Fig. 2(E), right), which represented a measure of the contrast of the image of the capillary vessels in the CC OCTA image.

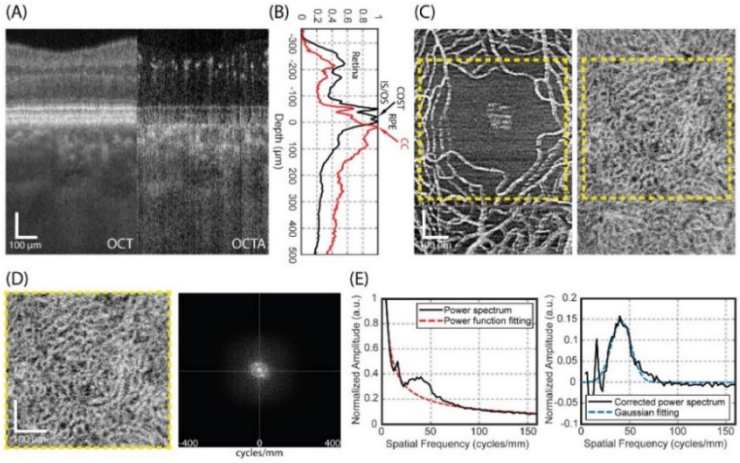

Fig. 2. OCTA image resulted from large probe beam size of 3.50 mm can resolve the individual capillary vessels in the CC at the posterior pole, providing an opportunity to quantify the CC integrity. (A) Cross-sectional OCT and OCTA images extracted from the volumetric data sets acquired at fovea in subject 3. (B) Normalized mean OCT and OCTA depth profiles of cross-sectional images in (A). The three most prominent peaks in the structure intensity profile (black) are inner/outer segment junction (IS/OS), cone outer segments tips (COST) and RPE. (C) *En-face* retina (left) and CC (right) OCTA images (FOV: ~0.6 × 0.8 mm^2). Yellow dashed frame indicates square area external to the vertexes of the FAZ for further comparison and morphology analysis. (D) cropped *en-face* CC OCTA image at FAZ (FOV: ~0.5 × 0.5 mm^2) and its corresponding 2D power spectrum. (E) Left: normalized radially-averaged power spectrum of *en-face* CC OCTA image at FAZ. The offset was fitted into power function (red dashed line). Right: Power spectrum of *en-face* CC OCTA image after offset removal and its corresponding Gaussian fitting. All scale bars: 100 μm.

Biomedical Optics EXPRESS

3. Results

3.1 SS-OCT transverse resolution

The OCT transverse resolution on the retina for three different beam diameters was evaluated by imaging the USAF 1951 resolution target with a phantom eye in the air. The resultant *en-face* projections of the resolution target for each beam diameter were generated by maximum intensity projection (MIP), as shown in Fig. 3(A-C). Each of them provides a field of view (FOV) of 1 × 1 mm^2 with a sampling spacing of ~0.57 µm/pixel. The zoomed-in views of the resolution patterns for groups 6 and 7 are shown on the right with a small FOV of 0.23 × 0.23 mm^2. Obviously, the clarity of the resolution patterns is increased with the increase of the diameter of incident beam. Note the artefacts at the edge of the resolution patterns imaged with smallest beam size (Fig. 3(A)) might be caused by the combination of laser spot diffraction occurring at the edge and astigmatism induced by the tilted incident beam.

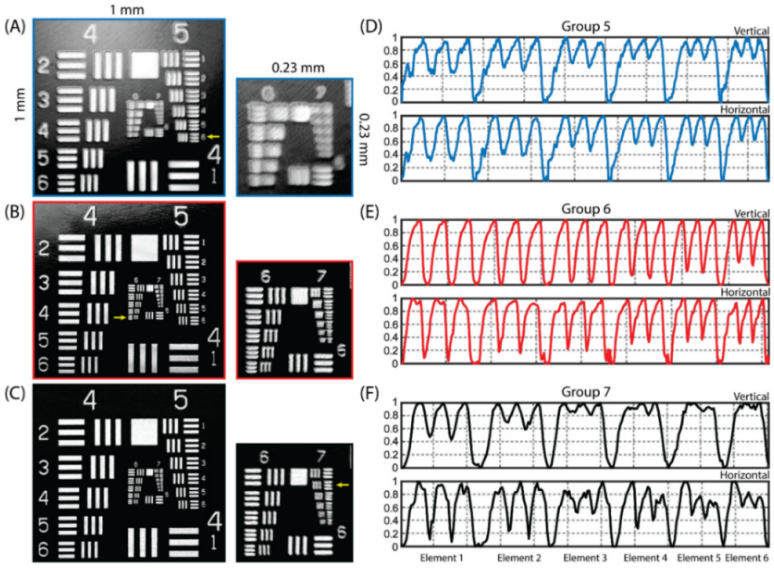

Fig. 3. The system transverse resolution was tested by the use of a standard USAF resolution target. (A-C) Resultant *en-face* images of the resolution target imaged with various beam diameters: A) 1.12 mm; B) 2.51 mm; and C) 3.50 mm, respectively. Small sub-frames on the right show the zoomed-in views for patterns of group 6 and 7. The small yellow arrows denote the minimum visually resolvable pattern for each beam size. (D) Normalized vertical (up) and horizontal (down) intensity profiles of USAF resolution target patterns (group 5) imaged by the beam diameter of 1.12 mm. (E) Normalized vertical (up) and horizontal (down) intensity profiles of USAF resolution target patterns (group 6) imaged by the beam diameter of 2.51 mm. (F) Normalized vertical (up) and horizontal (down) intensity profiles of USAF resolution target patterns (group 7) imaged by the beam diameter of 3.50 mm.

The normalized intensity profiles of vertical and horizontal USAF resolution target patterns for each beam diameter (group 5 for the beam diameter of 1.12 mm, group 6 for 2.51 mm beam diameter and group 7 for the 3.50 mm beam diameter) are shown in Fig. 3(D-F). The minimum resolvable pattern for each lens-set configuration was then judged based on these intensity profiles according to the Rayleigh criterion. Therefore, the smallest resolvable patterns for beam diameters of 1.12 mm, 2.51 mm, 3.50 mm were element 6 in group 5, element 6 in group 6 and element 2 in group 7 respectively, corresponding to the transverse resolution of 17.5 µm, 8.8 µm and 7.0 µm on the retina. The theoretical transverse resolution that this phantom eye can achieve with beam diameters of 1.12 mm, 2.51 mm and 3.50 mm was calculated using Eq. (2) to be 18.9 µm, 8.4 µm and 6.0 µm, respectively. The measured transverse resolution was nearly consistent with the theoretical ones. The poorer transverse

Biomedical Optics EXPRESS

resolution for the beam diameter of 3.50 mm may be attributed to the aberration caused by the imperfection of the lenses and the system alignment. However, the real transverse resolution on the retina would be worse than these estimated values because of the distortion and aberration caused by the imperfection of the cornea and the lens in the eye. For instance, a subject with a prescription containing cylinder needs astigmatism correction to be imaged at the diffraction-limited resolution, especially for the beam diameter of 3.50 mm.

3.2 CC OCTA results with different beam sizes

To evaluate the effect of system transverse resolution on the CC OCTA imaging, the CC of subject 1 was imaged with three different beam diameters at the same location. The results are shown in Fig. 4.

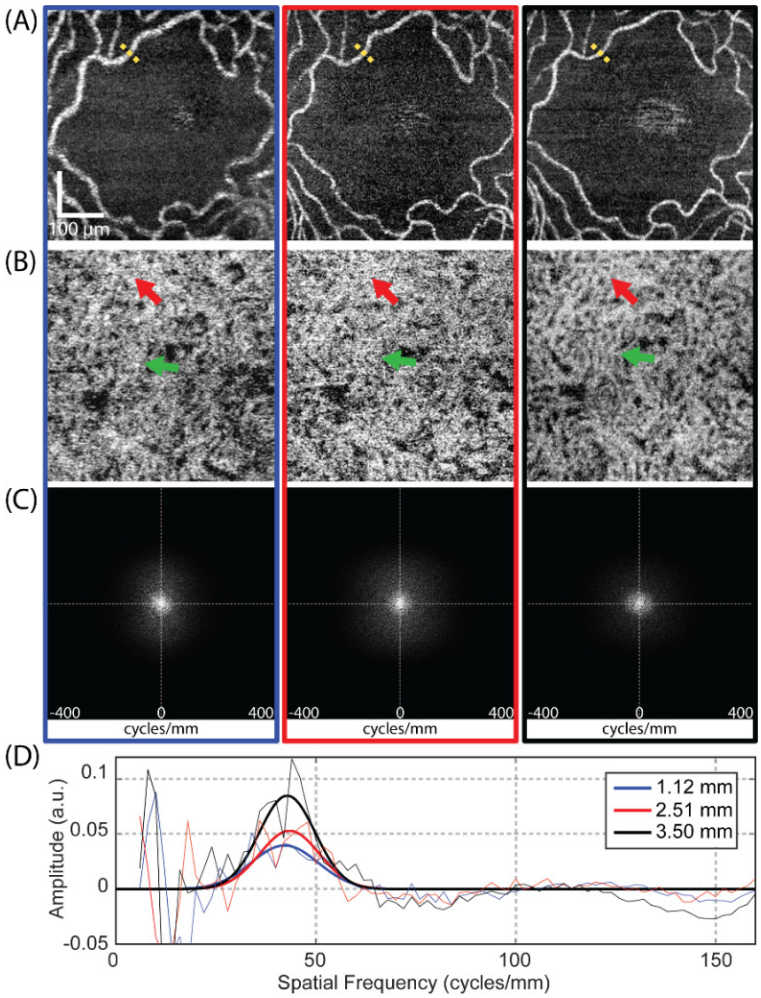

Fig. 4. The clarity of the OCTA vascular image is affected by the incident beam size. (A) *En-face* retina OCTA images at FAZ region imaged by the beam diameters of 1.12 mm, 2.51 mm and 3.50 mm (from left to right), respectively. (B) Corresponding *en-face* CC OCTA images. (C) 2D power spectrums of *en-face* CC OCTA images for all three beam diameters. (D) Offset-removed radially-averaged power spectrums of CC (solid line, thin, blue for the beam diameter of 1.12 mm, red for the beam diameter of 2.51 mm and black for the beam diameter of 3.50 mm) and their corresponding Gaussian fitting curves (solid line, bold).

As a first qualitative comparison, the vessels appear thicker in *en-face* retina OCTA images acquired with the small beam size than that with the larger beam size (Fig. 4(A)),

Biomedical Optics EXPRESS

which is also confirmed by manually measured vessel diameters at the locations indicated by the dashed yellow lines (16.7 μm for the beam diameter of 1.12 mm, 9.2 μm for the beam diameter of 2.51 mm and 9.0 μm for the beam diameter of 3.50 mm). Therefore, although individual retinal vessels are visualized for all beam sizes, the vessel diameter looks broader with the small beam size due to the lower transverse resolution (larger spot size) on the retina. The same effect occurs in *en-face* CC OCTA results as well, as shown in Fig. 4(B). The CC vessels imaged with the beam diameter of 1.12 mm also look much thicker than that with the beam diameter of 3.50 mm. Therefore, details of the fine CC lobular network that cannot be discriminated with the small beam sizes can be visualized clearly with the large beam size, as indicated by the red and green arrows in this figure.

For quantitatively analyzing the CC OCTA results, 2D power spectrum analysis was applied onto each *en-face* CC angiogram. Figure 4(C, D) show the 2D power spectrums of the *en-face* CC angiograms for all three beam sizes and their corresponding offset-removed radially-averaged power spectrums. The magnitude of the CC peak in radially-averaged power spectrums were measured to be 0.040, 0.053 and 0.085 for the beam diameters of 1.12 mm, 2.51 mm and 3.50 mm, corresponding to a 114% higher image contrast in the CC angiogram imaged with the largest beam diameter than that with the smallest beam diameter. Therefore, the larger beam size (high transverse resolution) provides higher image contrast in the CC OCTA image, as expected.

The CC spatial frequencies were estimated by fitting the offset-removed radially-averaged power spectrum into a Gaussian function, which gave the estimated values of 42.2 cycles/mm, 43.5 cycles/mm and 42.9 cycles/mm for the beam diameters of 1.12 mm, 2.51 mm and 3.50 mm, corresponding to mean CC inter-vascular spacings of 23.5 μm, 23.0 μm and 23.3 μm, respectively. The corresponding bandwidths of the CC spatial frequencies could also be extracted from the Gaussian fittings to be 11.9 cycles/mm, 10.6 cycles/mm and 9.9 cycles/mm, indicating the reduction in the variance of the estimated CC inter-vascular spacings with the increase of the beam size. Therefore, the larger beam size (high transverse resolution) provides more accurate and stable CC inter-vascular spacing estimation, as expected.

The mean RPE-CC distance of three different beam diameters were measured as well, to be 18.2 ± 1.5 μm (1.12 mm), 17.9 ± 1.1 μm (2.51 mm) and 17.9 ± 1.1 μm (3.50 mm). The variance between them was ~1.4%, less than 5%. This result is encouraging, because it indicates that the different beam sizes do not influence the quantification of the RPE-CC distance.

3.3 CC OCTA results for all subjects

After exploring the effect of probe beam size on the CC imaging, the largest beam size (3.50 mm) was applied on three additional subjects to test the flexibility and robustness of the proposed CC visualization approach. The results are shown in Fig. 5. All the *en-face* CC angiograms give a good visualization of the CC lobular vessel network at the FAZ region (Fig. 5 (A)).

The mean RPE-CC distance (Fig. 5(B)) was measured to be 17.9 ± 1.1 μm, 18.7 ± 0.7 μm, 20.0 ± 1.1 μm, and 20.3 ± 1.0 μm for subject 1, 2, 3 and 4, respectively, which agreed well with those from previous studies (from 16 to 31 μm) [17] and other measurements from SS-OCT (17.3 μm) [13] and AO-OCT (17.5 ± 2.1 μm) [14].

The mean CC inter-vascular spacing (Fig. 5(C)) was estimated to be 23.2 ± 1.1 μm, 24.5 ± 0.4 μm, 24.4 ± 0.5 μm, and 25.4 ± 0.1 μm for 4 subjects respectively. The measured CC spacing matches with our previous results (21.05 – 25.28 μm) [17] very well. However, it is smaller than the reported value from SS-OCT (34.77 ± 4.67) [13,38] and AO-OCT (39 μm) [14], which could be due to variations among individual subjects.

Biomedical Optics EXPRESS

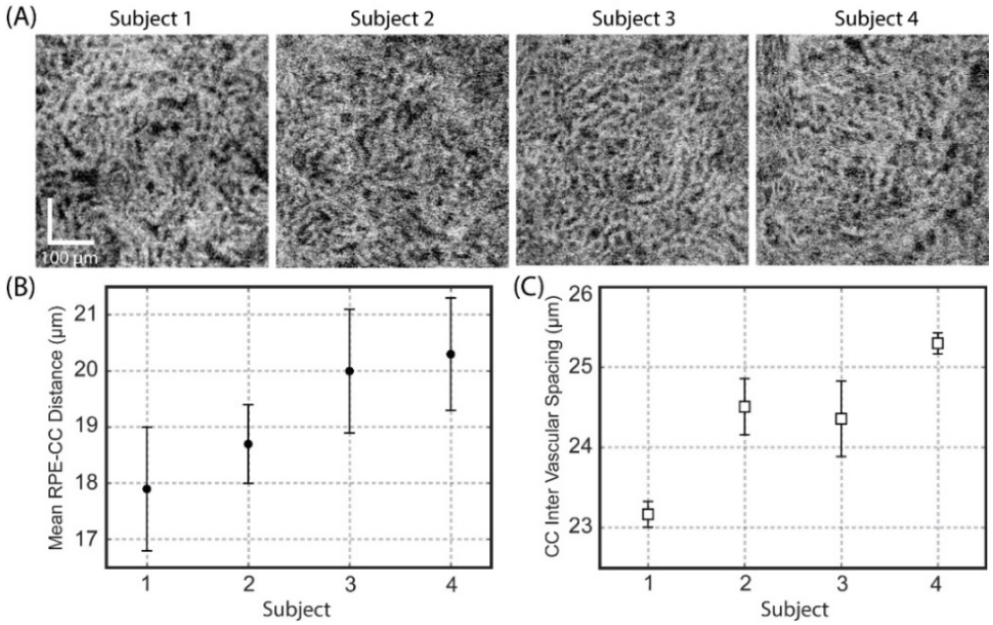

Fig. 5. The choriocapillaris lobular network under the central fovea region can be resolved by a commercial grade SS-OCT system with an incident probe beam diameter of ~3.50 mm at the pupil plane. (A) *En-face* OCTA images of the CC slab at the posterior pole region acquired from 4 normal subjects. (B) Measured mean RPE-CC distance (mean ± std) of the 4 subjects. (C) Measured mean CC inter-vascular spacing (mean ± std) of the subjects.

4. Discussion

In this study, the effect of various probe beam sizes on the ability of CC OCTA to resolve the lobular capillary network under the posterior pole region has been investigated. The results show that for a conventional OCTA system with features similar to current commercial SS-OCT systems (200 kHz A-line rate, 4 repeated B-scans), the probe beam size at the pupil plane is a key parameter for CC angiography if the purpose of the investigation is to visualize the individual capillaries. This conclusion is relatively straightforward since we know from the Gaussian optics, the entry optical beam size before any objective lens (numerical aperture) determines the transverse resolution of the system. The three beam sizes used in this study were 1.12 mm, 2.51 mm and 3.50 mm, which provided corresponding nominal system transverse resolution of ~17.5 µm, ~8.8 µm and ~7.0 µm, respectively, at the retina. The CC lobular capillary network was resolved in angiograms with increased imaging contrast and clarity when the probe beam size was increased. The contrast of the CC angiogram with a large beam size of 3.50 mm was up to 114% higher than that with a small beam size of 1.12 mm. Therefore, in a conventional OCTA system with fixed scan speed, repeated B-scan number and scan density, the beam size is a dominant parameter for visualizing the individual capillary vessels in the CC network.

When quantifying CC morphometric parameters, the larger beam size provided reduced variance (standard deviation) in the measurements of mean RPE-CC distance and CC inter-vascular spacing, indicating more reliable and stable ability for quantification. However, when compared to the beam size of 3.50 mm, we noticed that a small beam size of 1.12 mm still provided comparable quantification results for both mean RPE-CC distance (17.9 ± 1.1 µm vs 18.2 ± 1.5 µm) and CC inter-vascular spacing (23.3 µm vs 23.0 µm). This observation is surprising and in fact clinically important because it indicates that the current commercial SS-OCTA systems, which typically have an entry beam size of ~1.2 mm at the pupil plane, might be still clinically useful in providing quantifiable information about the CC network.

Biomedical Optics EXPRESS

While at ~1.2 mm beam size it is difficult to resolve the individual capillary vessels at the posterior pole, the commercial systems would be sufficient to discriminate the flow deficits at the CC. By definition, the flow deficit must be larger in size than the inter-capillary distance (typically about 24 μm [20]), which should be well within the capability of the commercial system to resolve. Due to these attributes, commercial systems have recently demonstrated clinical utility in a number of investigations of eye diseases that are thought to be involved with CC flow deficits [17,20].

While we have demonstrated the effect of probe beam size on the ability of the OCTA system to resolve the CC capillary vessels, there are some other important factors that may play a role in this endeavor. Among them, the scan speed (A-line rate) of OCTA system is an important parameter for choriocapillaris visualization since the high scan speed can provide OCTA imaging with high scan density and more repeated B-scans without increasing (or even reducing) the total data acquisition time. Such attributes from the high scan speed are not only helpful to increase the image contrast of CC angiography, but also important for suppressing the bulk motion artifacts in the CC angiography [13,38]. While the drawbacks of high scan speed system are the reduced system sensitivity and the increased costs, especially for the laser source. The SS-OCT system with 200 kHz A-line rate used in this study is already fast enough to provide us with a high-quality CC angiogram within a total data acquisition time of 4.8 s. More important, SS-OCTA commercial system with an imaging speed of 200 kHz is currently pending FDA approval.

The number of repeated B-scans also affects the blood flow contrast of the resultant angiogram. For an OCTA system with stable phase, more repeated B-scans leads to the better blood flow contrast [7]. Thus, the more repeated B-scans that can be afforded for averaging, the lower the system background noise would be. In this investigation, we used four as the repeated B-scan number to be consistent with the commercially available OCTA systems.

Another important parameter that could influence the image contrast of CC angiography is the number of A-scans within one B-scan, i.e. scan density. Higher scan density improves the appearance of resultant angiography as reported in Gorczynska's work [13,38]. The scan densities used in this study for three different beam sizes were unusually high when compared to others, which were 8.8x, 4.4x, 3.5x times denser for the beam diameters of 1.12 mm, 2.51mm and 3.50 mm, respectively. All of them meets the Nyquist–Shannon sampling theorem. However, with limited system transverse resolution, e.g. ~17.5 μm with 1.12 mm beam diameter, fine CC lobular network still cannot be discriminated even with 8.8x oversampling ratio. Therefore, the scan density helps improve the image contrast of CC angiogram, but not necessarily the dominant factor for CC visualization.

There are also some important limitations for this study. First, the large beam size would reduce the depth of focus (DOF). The depth of focus can be estimated through the following expression [39]:

$$DOF_{Z_{OCT}} = 2Z_R = \frac{2\pi \cdot \Delta x^2}{\lambda_c} \tag{3}$$

where Z_R denotes the Rayleigh range of Gaussian optics, Δx represents the system transverse resolution and λ_c is the center wavelength of the laser source. Thus, the nominal DOF of three beam sizes are calculated to be 1833 μm, 463 μm and 293 μm, respectively. The typical thickness of the posterior segment of human eye is about 600 μm (Fig. 2(B)), therefore, the DOF of large beam size is not able to cover the entire retina and choroid, and the tissue outside the Rayleigh range will become defocused. However, for the specific application to enhance CC visualization, the Rayleigh range is still long enough to cover the thin CC layer (~15 – 20 μm thickness), even for the largest beam diameter of 3.50 mm investigated in this study. Second, the large beam size may cause diffraction on the edge of pupil. All subjects were imaged without eye dilation but in a dark room with low environment light. It is likely

Biomedical Optics EXPRESS

that the edge of pupil would induce diffraction errors if the pupil is not open wide enough to accommodate the large beam size, resulting in the deterioration of Gaussian beam and thus the system transverse resolution as well as the image contrast of the resultant CC angiogram. To mitigate this issue, the subject's pupil can be dilated. This is not an issue because pupil dilation is a routine procedure in the ophthalmic clinic for various clinical examinations of the eyes. A third limitation is the small field of view of the CC angiogram. The field of view in our study was chosen to be 0.6 mm × 0.8 mm, covering an area slightly larger than FAZ, for the reasons of balancing between the field of view and the total data acquisition time, and merely serving our purpose to demonstrate the effect of the increase of numerical aperture on the transverse resolution. For a large field of view imaging, such as 6 mm × 6 mm in a typical commercial system, it would take about 58 s to complete the scan on a 200 kHz A-line rate system (1700 A-line × 1700 frames × 4 repeats) with satisfying the requirement of high scan density (3.5 μm pixel pitch). It is a challenge even for a normal patient. However, this challenge may be mitigated by 1) reducing the total data acquisition time through a more efficient scan protocol, e.g. a bidirectional scan protocol, 2) minimizing motion artifacts with motion tracking mechanism built in the system, or 3) stitching several CC scans with small field of view as reported in Migacz's work [38].

5. Conclusion

In this paper, we have demonstrated the effect of probe beam size on system transverse resolution to improve the CC lobular vessel network visualization in the conventional OCTA system with features comparable to commercially available OCTA system. Three different beam diameters (1.12 mm, 2.51 mm and 3.50 mm) were employed to alter the system transverse resolution at the retina in an effort to resolve the CC capillary vessels at the posterior pole. Four subjects participated in this study. The results show that the beam size is a key parameter for CC angiography if the purpose of the investigation is to visualize the individual capillaries. The CC lobular capillary network was discriminated in angiograms provided by the large beam size of 3.50 mm. The image contrast of the CC angiogram with a beam size of 3.50 mm was up to 114% higher than that with a small beam size of 1.12 mm. The measurements of the mean RPE-CC distance and the CC inter-vascular spacing were also more reliable and stable with the large beam size. However, small beam size could still provide comparable quantification results for both morphometric parameters, e.g. mean RPE-CC distance and CC inter-vascular spacing, indicating the current commercial OCTA systems might be still applicable to providing useful information relevant to clinical measurements.

Funding

Washington Research Foundation; Research to Prevent Blindness.

Acknowledgments

Research supported in part by Washington Research Foundation, and an unrestricted grant from the Research to Prevent Blindness, Inc., New York, NY. The funding organizations had no role in the design or conduct of this research.

Disclosures

Dr. Wang discloses intellectual property owned by the Oregon Health and Science University and the University of Washington. Dr. Wang also receives research support from Colgate Palmolive Company, Carl Zeiss Meditec Inc, Tasso Inc, Moptim Inc, and Facebook technologies LLC. He is a consultant to Carl Zeiss Meditec, and Insight Photonic Solutions.

The remaining authors have no disclosures.

Biomedical Optics EXPRESS

References

1. H. R. Zhang, "Scanning electron-microscopic study of corrosion casts on retinal and choroidal angioarchitecture in man and animals," Prog. Retin. Eye Res. **13**(1), 243–270 (1994).
2. C. W. Spraul, G. E. Lang, H. E. Grossniklaus, and G. K. Lang, "Histologic and morphometric analysis of the choroid, Bruch's membrane, and retinal pigment epithelium in postmortem eyes with age-related macular degeneration and histologic examination of surgically excised choroidal neovascular membranes," Surv. Ophthalmol. **44**(Suppl 1), S10–S32 (1999).
3. A. Biesemeier, T. Taubitz, S. Julien, E. Yoeruek, and U. Schraermeyer, "Choriocapillaris breakdown precedes retinal degeneration in age-related macular degeneration," Neurobiol. Aging **35**(11), 2562–2573 (2014).
4. D. S. McLeod and G. A. Lutty, "High-resolution histologic analysis of the human choroidal vasculature," Invest. Ophthalmol. Vis. Sci. **35**(11), 3799–3811 (1994).
5. C. W. Spraul, G. E. Lang, H. E. Grossniklaus, and G. K. Lang, "Morphometric changes in the choriocapillaris and choroid in eyes with advanced glaucoma damage," Ophthalmologe **97**(10), 663–668 (2000).
6. A. Zhang, Q. Zhang, C.-L. Chen, and R. K. Wang, "Methods and algorithms for optical coherence tomography-based angiography: a review and comparison," J. Biomed. Opt. **20**(10), 100901 (2015).
7. C.-L. Chen and R. K. Wang, "Optical coherence tomography based angiography [Invited]," Biomed. Opt. Express **8**(2), 1056–1082 (2017).
8. W. Choi, K. J. Mohler, B. Potsaid, C. D. Lu, J. J. Liu, V. Jayaraman, A. E. Cable, J. S. Duker, R. Huber, and J. G. Fujimoto, "Choriocapillaris and choroidal microvasculature imaging with ultrahigh speed OCT angiography," PLoS One **8**(12), e81499 (2013).
9. L. An and R. K. Wang, "In vivo volumetric imaging of vascular perfusion within human retina and choroids with optical micro-angiography," Opt. Express **16**(15), 11438–11452 (2008).
10. L. An, H. M. Subhush, D. J. Wilson, and R. K. Wang, "High-resolution wide-field imaging of retinal and choroidal blood perfusion with optical microangiography," J. Biomed. Opt. **15**(2), 026011 (2010).
11. R. K. Wang, L. An, P. Francis, and D. J. Wilson, "Depth-resolved imaging of capillary networks in retina and choroid using ultrahigh sensitive optical microangiography," Opt. Lett. **35**(9), 1467–1469 (2010).
12. C. Rochepeau, L. Kodjikian, M.-A. Garcia, C. Coulon, C. Burillon, P. Denis, B. Delaunay, and T. Mathis, "Optical Coherence Tomography Angiography Quantitative Assessment of Choriocapillaris Blood Flow in Central Serous Chorioretinopathy," Am. J. Ophthalmol. **194**, 26–34 (2018).
13. I. Gorczynska, J. Migacz, R. Jonnal, R. Zawadzki, R. Poddar, and J. Werner, "Imaging of the human choroid with a 1.7 MHz A-scan rate FDML swept source OCT system," in *Ophthalmic Technologies XXVII*, (International Society for Optics and Photonics, 2017), 1004510.
14. K. Kurokawa, Z. Liu, and D. T. Miller, "Adaptive optics optical coherence tomography angiography for morphometric analysis of choriocapillaris," Biomed. Opt. Express **8**(3), 1803–1822 (2017).
15. D. Y. Kim, J. Fingler, R. J. Zawadzki, S. S. Park, L. S. Morse, D. M. Schwartz, S. E. Fraser, and J. S. Werner, "Optical imaging of the chorioretinal vasculature in the living human eye," Proc. Natl. Acad. Sci. U.S.A. **110**(35), 14354–14359 (2013).
16. Q. Zhang, F. Zheng, E. H. Motulsky, G. Gregori, Z. Chu, C.-L. Chen, C. Li, L. de Sisternes, M. Durbin, P. J. Rosenfeld, and R. K. Wang, "A Novel Strategy for Quantifying Choriocapillaris Flow Voids Using Swept-Source OCT Angiography," Invest. Ophthalmol. Vis. Sci. **59**(1), 203–211 (2018).
17. Z. Chu, H. Zhou, Y. Cheng, Q. Zhang, and R. K. Wang, "Improving visualization and quantitative assessment of choriocapillaris with swept source OCTA through registration and averaging applicable to clinical systems," Sci. Rep. **8**(1), 16826 (2018).
18. M. Al-Sheikh, N. Phasukkijwatana, R. Dolz-Marco, M. Rahimi, N. A. Iafe, K. B. Freund, S. R. Sadda, and D. Sarraf, "Quantitative OCT angiography of the retinal microvasculature and the choriocapillaris in myopic eyes," Invest. Ophthalmol. Vis. Sci. **58**(4), 2063–2069 (2017).
19. Y. Teng, M. Yu, Y. Wang, X. Liu, Q. You, and W. Liu, "OCT angiography quantifying choriocapillary circulation in idiopathic macular hole before and after surgery," Graefes Arch. Clin. Exp. Ophthalmol. **255**(5), 893–902 (2017).
20. Q. Zhang, Y. Shi, H. Zhou, G. Gregori, Z. Chu, F. Zheng, E. H. Motulsky, L. de Sisternes, M. Durbin, P. J. Rosenfeld, and R. K. Wang, "Accurate estimation of choriocapillaris flow deficits beyond normal intercapillary spacing with swept source OCT angiography," Quant. Imaging Med. Surg. **8**(7), 658–666 (2018).
21. P. L. Nesper, P. K. Roberts, A. C. Onishi, H. Chai, L. Liu, L. M. Jampol, and A. A. Fawzi, "Quantifying microvascular abnormalities with increasing severity of diabetic retinopathy using optical coherence tomography angiography," Invest. Ophthalmol. Vis. Sci. **58**(6), BIO307 (2017).
22. N. Jain, Y. Jia, S. S. Gao, X. Zhang, R. G. Weleber, D. Huang, and M. E. Pennesi, "Optical coherence tomography angiography in choroideremia: correlating choriocapillaris loss with overlying degeneration," JAMA Ophthalmol. **134**(6), 697–702 (2016).
23. P. L. Nesper, B. T. Soetikno, and A. A. Fawzi, "Choriocapillaris nonperfusion is associated with poor visual acuity in eyes with reticular pseudodrusen," Am. J. Ophthalmol. **174**, 42–55 (2017).
24. M. Lane, E. M. Moult, E. A. Novais, R. N. Louzada, E. D. Cole, B. Lee, L. Husvogt, P. A. Keane, A. K. Denniston, A. J. Witkin, C. R. Baumal, J. G. Fujimoto, J. S. Duker, and N. K. Waheed, "Visualizing the choriocapillaris under drusen: comparing 1050-nm swept-source versus 840-nm spectral-domain optical coherence tomography angiography," Invest. Ophthalmol. Vis. Sci. **57**(9), OCT585 (2016).

Biomedical Optics EXPRESS

25. Y. Kuroda, S. Ooto, K. Yamashiro, A. Oishi, H. Nakanishi, H. Tamura, N. Ueda-Arakawa, and N. Yoshimura, "Increased choroidal vascularity in central serous chorioretinopathy quantified using swept-source optical coherence tomography," Am. J. Ophthalmol. **169**, 199–207 (2016).
26. A. Carnevali, R. Sacconi, E. Corbelli, L. Tomasso, L. Querques, G. Zerbini, V. Scorcia, F. Bandello, and G. Querques, "Optical coherence tomography angiography analysis of retinal vascular plexuses and choriocapillaris in patients with type 1 diabetes without diabetic retinopathy," Acta Diabetol. **54**(7), 695–702 (2017).
27. A. W. Fryczkowski, "Anatomical and functional choroidal lobuli," Int. Ophthalmol. **18**(3), 131–141 (1994).
28. J. Polans, D. Cunefare, E. Cole, B. Keller, P. S. Mettu, S. W. Cousins, M. J. Allingham, J. A. Izatt, and S. Farsiu, "Enhanced visualization of peripheral retinal vasculature with wavefront sensorless adaptive optics optical coherence tomography angiography in diabetic patients," Opt. Lett. **42**(1), 17–20 (2017).
29. J. Polans, B. Keller, O. M. Carrasco-Zevallos, F. LaRocca, E. Cole, H. E. Whitson, E. M. Lad, S. Farsiu, and J. A. Izatt, "Wide-field retinal optical coherence tomography with wavefront sensorless adaptive optics for enhanced imaging of targeted regions," Biomed. Opt. Express **8**(1), 16–37 (2017).
30. R. Maddipatla, J. Cervantes, Y. Otani, and B. Cense, "Retinal imaging with optical coherence tomography and low-loss adaptive optics using a 2.8-mm beam size," J. Biophotonics **2018**, e201800192 (2018).
31. P. H. Tomlins and R. Wang, "Theory, developments and applications of optical coherence tomography," J. Phys. D Appl. Phys. **38**(15), 2519–2535 (2005).
32. D. Palanker, "Optical Properties of the Eye," AAO One Network (2013).
33. H. Wang, J. Izatt, and M. Kulkarni, "Handbook of Optical Coherence Tomography ed BE Bouma and GJ Tearney," (New York: Dekker, 2002), pp. 275–298.
34. A. N. S. Institute, *American National Standard for Safe use of Lasers* (Laser Institute of America, 2007).
35. X. Yin, J. R. Chao, and R. K. Wang, "User-guided segmentation for volumetric retinal optical coherence tomography images," J. Biomed. Opt. **19**(8), 086020 (2014).
36. Z. Chu, C.-L. Chen, Q. Zhang, K. Pepple, M. Durbin, G. Gregori, and R. K. Wang, "Complex signal-based optical coherence tomography angiography enables in vivo visualization of choriocapillaris in human choroid," J. Biomed. Opt. **22**(12), 1–10 (2017).
37. D. J. Moore and G. M. Clover, "The effect of age on the macromolecular permeability of human Bruch's membrane," Invest. Ophthalmol. Vis. Sci. **42**(12), 2970–2975 (2001).
38. J. V. Migacz, I. Gorczynska, M. Azimipour, R. Jonnal, R. J. Zawadzki, and J. S. Werner, "Megahertz-rate optical coherence tomography angiography improves the contrast of the choriocapillaris and choroid in human retinal imaging," Biomed. Opt. Express **10**(1), 50–65 (2019).
39. M. Pircher and R. J. Zawadzki, "Review of adaptive optics OCT (AO-OCT): principles and applications for retinal imaging," Biomed. Opt. Express **8**(5), 2536–2562 (2017).